Daytime measurements of atmospheric temperature profiles (2–15 km) by lidar utilizing Rayleigh–Brillouin scattering

Benjamin Witschas,* Christian Lemmerz, and Oliver Reitebuch

Deutsches Zentrum für Luft- und Raumfahrt (DLR), Institut für Physik der Atmosphäre, Oberpfaffenhofen 82234, Germany
Corresponding author: Benjamin.Witschas@dlr.de

In this Letter, we report on a novel method for measuring atmospheric temperature profiles by lidar during daytime for heights of 2–15.3 km, with a vertical resolution of 0.3–2.2 km, using Rayleigh–Brillouin scattering. The measurements are performed by scanning a laser ($\lambda = 355$ nm) over a 12 GHz range and using a Fabry–Pérot interferometer as discriminator. The temperature is derived by using a new analytical line shape model assuming standard atmospheric pressure conditions. Two exemplary temperature profiles resulting from measurements over 14 and 27 min are shown. A comparison with radiosonde temperature measurements shows reasonable agreement. In cloud-free conditions, the temperature difference reaches up to 5 K within the boundary layer, and is smaller than 2.5 K above. The statistical error of the derived temperatures is between 0.15 and 1.5 K.   © 2014 Optical Society of America

OCIS codes: (280.3640) Lidar; (280.1310) Atmospheric scattering; (280.6780) Temperature.
http://dx.doi.org/10.1364/OL.39.001972

Observational data on atmospheric temperature profiles are important inputs to models predicting the atmospheric state or to retrieve details of other atmospheric properties, such as wind, pressure, relative humidity, or other trace gas concentrations. Currently, lidar instruments enable the measurement of temperature with high accuracy (≈ 1 K), high vertical resolution (≈ 100 m), and long range (from ground up to 105 km) [1].

For tropospheric temperature profiling, it is common to make use of rotational Raman scattering on air molecules [2–4], whereby the temperature dependence of the intensities of rotational Raman lines is exploited. At date, rotational Raman lidars provide tropospheric temperature measurements with high temporal and spatial resolution. For instance Radlach *et al.* [3] demonstrated daytime measurements from ground up to 5 km with a temporal resolution of 60 s and an uncertainty below 1 K from ground up to 1 km. During the night, temperatures with an uncertainty below 1 K were derived up to 14 km by applying an integration time of 60 min and a gliding average of 750 m. Behrendt and Reichardt [4] further showed that rotational Raman lidars can be used to profile temperature also in the presence of clouds up to a backscatter ratio of 45. In addition, it was discussed that even airborne [5] and space-borne [6] applications of the Raman technique are feasible.

Nevertheless, it has to be mentioned that the Raman scattering cross section is quite low. Thus, powerful lasers, sophisticated background filters, or night-time operation are required to obtain reliable results. In particular, the rotational Raman scattering cross section (considering Stokes and anti-Stokes branches) is about a factor of 53 smaller than the one of Rayleigh scattering [7]. Regarding this, it would be beneficial to derive temperatures from Rayleigh–Brillouin (RB) scattering, which can be done by high spectral resolution lidars (HSRL).

Generally speaking, temperature is a measure of the average kinetic energy of molecules, which has its imprint within the RB spectrum. Thus, atmospheric temperature can be derived by resolving the RB spectrum with high spectral resolution filters, such as atomic vapor cells or Fabry–Pérot interferometers (FPIs), and relating the measured spectrum to an appropriate line shape model. The narrow RB line width of a few GHz additionally enables the application of narrow band filters that suppress solar radiation and, thus, enable daytime operation.

Up to now, a few attempts of measuring temperature with HSRL have been performed. Schwiesow and Lading [8] introduced an approach of measuring atmospheric temperature profiles by means of two Michelson interferometers, although without any practical success. The first measured temperature profiles from 1 km to 5 km (375 m vertical resolution) were reported by She *et al.* [9] and Alvarez *et al.* [10]. They used a dye laser and a barium absorption cell to separate the molecular signal from the aerosol signal and applied the Tenti line shape model [11] for temperature retrieval. In 2001, Hair *et al.* [12] reported on HSRL measurements performed with a frequency doubled Nd:YAG laser and an iodine absorption filter. They derived vertical temperature profiles between 0.5 and 15 km (300 m horizontal resolution), which agreed with radiosonde profiles within 2 K over an altitude range of 2–5 km. The uncertainty was estimated to be at maximum 9.7 K. Hua *et al.* [13] introduced a Rayleigh–Mie lidar for daytime temperature profiling, using a frequency tripled Nd:YAG laser and, for the first time, a double-edge FPI. They showed temperature profiles from ground up to 4 km and calculated the uncertainty to be less than 1 K.

The overview given above shows that, except for that of Hua *et al.*, all HSRL systems used vapor absorption cells to get information from the RB signal. Due to the spectral characteristics of absorption lines, the resolution of these systems is coarse, requiring the definition of response functions, calibration procedures, as well as the assumption of hydrostatic equilibrium for temperature retrieval. Furthermore, it is difficult to arrange

absorption cells for short wavelengths that would be favorable, due to the λ^{-4}-proportionality of the Rayleigh scattering cross section. Operating at UV wavelengths also leaves fewer constraints due to eye-safety for ground-, air-, and space-borne lidar operations. In addition, the application of high-resolution interferometers would provide a higher resolution of the RB line shape, leading to better accuracy and a reduction of the required measurement time.

Considering the discussion above, we suggest a novel approach for HSRL temperature measurements based on resolving the RB line shape by means of an interferometer with high spectral resolution and relating it to an analytical line shape model [14,15], which uses standard atmospheric pressures and, additionally, considers particle scattering. Here, RB and particle scattering is not separated in different channels as it is commonly done with HSRL, but information is gained from the different imprints in the measured spectrum. Furthermore, temperature values derived at different altitudes are independent of each other, as no response function has to be used for the retrieval. Additionally, the suggested approach yields absolute temperature values without applying any calibration procedure. This is demonstrated on two exemplary atmospheric daytime measurements from 2 to 15.3 km compared with radiosonde temperature profiles. To our knowledge, this is the first time that temperature profiles up to this altitude have been measured during daytime with an averaging time of 14 min by utilizing RB scattering.

The lidar used in this study was not originally built for this purpose, but is actually a Doppler wind lidar, which validates the instrument of the ADM-Aeolus satellite mission initiated by ESA [16]. However, as it is shown here, the instrument is also suited for measuring temperature by means of RB scattering. Possible improvements of the given setup for future instruments are discussed at the end of this Letter. Here, only the setup components that are important for this study are shortly discussed (Fig. 1). More information is given in [17,18].

The laser transmitter consists of an injection-seeded, frequency-tripled, diode-pumped and pulsed Nd:YAG laser with an output energy of 60 mJ/pulse, a pulse repetition rate of 50 Hz and a line width of 50 MHz (full width half-maximum (FWHM)) at 354.89 nm (844.754 THz). The seed laser in the reference laser head (Innolight GmbH) delivers frequency-tunable continuous wave radiation with high frequency stability (234 kHz RMS) and can
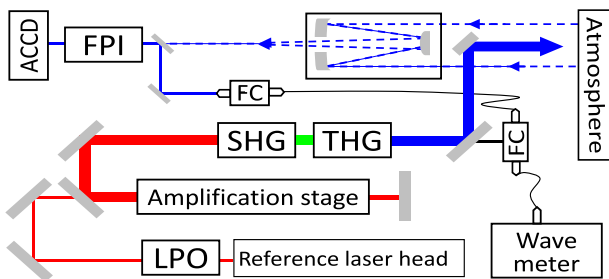
be set to a user-defined frequency. This enables tuning the laser frequency over a range of 12 GHz, which is needed to sample the RB spectrum. The seed laser is coupled into a low-power oscillator (LPO), which yields, after amplification and second and third harmonic generation (SHG, THG), laser pulses with 60 mJ. A part of the UV light is coupled into a fiber coupler (FC) and directed to a wavelength meter (High Finesse, WSU 10), which allows measurement of the absolute frequency with an accuracy of 2 MHz by further calibrating to a He–Ne laser.

The light backscattered from the atmosphere is collected with a Cassegrain telescope, which consists of a 200 mm primary mirror and a 75 mm secondary mirror with a focal length of 1.5 m, and then sent to the receiver. The receiver consists of a field stop, to set the field-of-view (FOV) to 100 μrad, an electro-optical modulator, which blocks the strong backscatter signal close to the instrument, and an FPI [FWHM = 1.7 GHz, free spectra range (FSR) = 10.9 GHz], which is used to resolve the RB spectrum. The light passing through the FPI is detected with an accumulation charge-coupled device (ACCD).

To obtain the resolved RB spectrum, the laser frequency is changed, in defined frequency steps Δf (e.g., $\Delta f = 125$ MHz or 250 MHz), over a range of 12 GHz (at 354.89 nm). For each frequency step, one observation consists of 700 pulses and takes 14 s. It takes additional 4 s to change the laser frequency, during which no measurement data is acquired. Considering 90/45 steps and a duration of 18 s per frequency step, the sampling of the entire RB line shape requires 27/14 min. It is worth mentioning that sampling the RB spectrum with only a few points ($\approx$15) would be enough to reach maximum accuracy for the temperature retrieval. However, as the measurement uncertainty is proportional to the signal level (see also Eq. (4)) reducing the sample number, or rather measurement time increases the uncertainty of the derived temperature values. Furthermore, it is beneficial to have more samples and, thus, higher resolution to resolve the peak resulting from particle scattering in aerosol-rich regions.

An example of measured RB line shapes ($\Delta f = 250$ MHz) at different distances (6.4–12.7 km) is shown in Fig. 2. It is pointed out that the signal from

Fig. 1.   Sketch of the lidar setup. LPO, low power oscillator; SHG and THG, second and third harmonic generation; FPI, Fabry–Pérot interferometer; ACCD, accumulation charged coupled device; FC, fiber coupler.
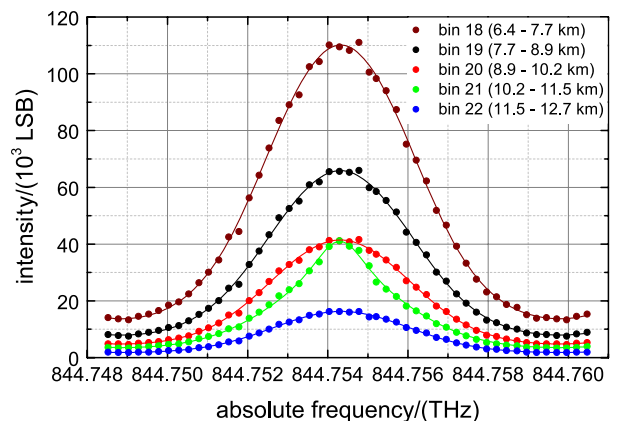

Fig. 2.   Measured RB line shapes for different distances from the lidar (dots) and best-fits using Eq. 1 (lines).

bin 21 (10.2–11.5 km) shows a remarkable contribution from significantly narrower particle scattering on a cirrus cloud, which also has to be considered for temperature retrieval.

Basically, the measured line shape $\mathcal{M}$ is the convolution of the spectral line shape of the laser $\mathcal{I}$, the FPI transmission function $\mathcal{A}$, and the spectral distribution of the received light $\mathcal{S}$ according to

$$\mathcal{M}(f) = \mathcal{I}(f) * \mathcal{A}(f) * \mathcal{S}(T, p, f), \qquad (1)$$

where $*$ denotes the convolution, f the optical frequency, and T and p the atmospheric temperature and pressure. Thus, accurate knowledge about $\mathcal{I}$, $\mathcal{A}$, and $\mathcal{S}$ is essential to avoid systematic errors in retrieving T. For this reason, the instrument function $\mathcal{T}(f) = \mathcal{I}(f) * \mathcal{A}(f)$ is measured simultaneously and modeled as discussed in [7]:

$$\mathcal{T}(f) = \frac{1}{\Gamma_{\text{FSR}}} \left(1 + 2 \sum_{k=1}^{\infty} R^k \cos\left(\frac{2\pi k f}{\Gamma_{\text{FSR}}}\right) \exp\left(-\frac{2\pi^2 k^2 \sigma_g^2}{\Gamma_{\text{FSR}}^2}\right) \right), \qquad (2)$$

where $\Gamma_{\text{FSR}} = 10934$ MHz is the FSR, $R = 0.66$ is the mirror reflectivity, and $\sigma_g = 287$ MHz is the defect parameter, taking mirror defects into account [18]. After having accurately described $\mathcal{T}$, the remaining spectrum $\mathcal{S}$ of the backscattered light has to be characterized. In the case of only considering RB scattering on air molecules, the line shape is appropriately described by the Tenti S6 line shape model [11], as shown by [18–20]. If aerosols are present, then particle scattering occurs and leads to an additional spectral component, which is similar to the spectral distribution of the laser pulse. Thus, for the temperature retrieval, $\mathcal{S}$ is described according to

$$\mathcal{S}(T, p, f) = I_{\text{mol}} \cdot \mathcal{S}_{\text{mol}}(T, p, f) + I_{\text{par}} \cdot \mathcal{S}_{\text{par}}(f), \qquad (3)$$

where $\mathcal{S}_{\text{mol}}(T, p, f)$ is the RB line shape normalized to unit area described by a parameterized version of the Tenti model according to Witschas [14,15] to enable analytical fit procedures, $\mathcal{S}_{\text{par}}(f)$ is a Dirac delta function, as no broadening for particle scattering is considered, and I_{mol} and I_{par} are the intensities of the RB signal and the particle signal, respectively. Hence, by applying a least squares fit procedure to Eq. 1 (including Eqs. 2 and 3), atmospheric temperature is derived (Fig. 2, lines). It is worth mentioning that atmospheric pressure is taken from the standard atmosphere, as the fit would not be stable for determining p and T simultaneously. This approach is justifiable, as simulations show that pressure deviations between standard atmosphere and real pressure of ± 10 hPa would lead to systematic errors of less than 0.1 K. Thus, the free fit parameters are T via $\mathcal{S}_{\text{mol}}(T, p, f)$, I_{mol} and I_{par}. This means that, in addition to T, an estimate about the backscatter ratio can be obtained by means of $(I_{\text{par}} + I_{\text{mol}})/(I_{\text{mol}})$.

The functionality of this retrieval procedure is demonstrated by means of two exemplary measurements. The temperature profiles shown in Fig. 3 (red dots) were derived from measurements performed on October 4, 2010 (12:20–13:31 UTC) at Oberpfaffenhofen, Germany. The
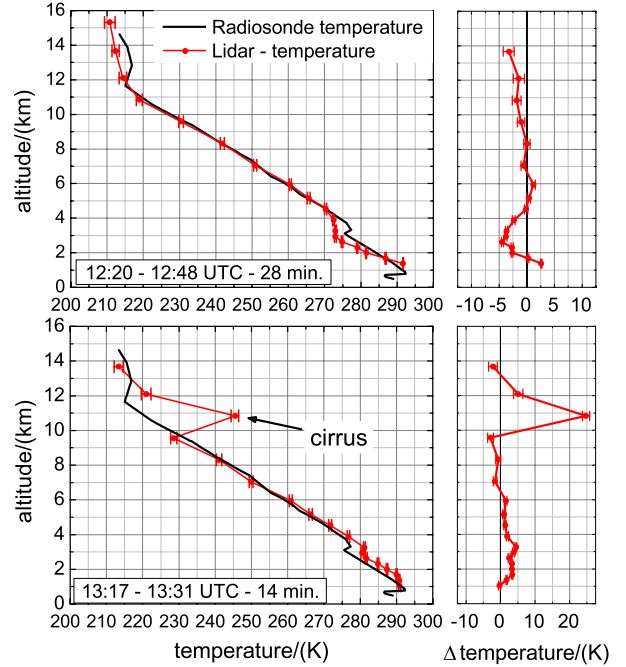

Fig. 3. Left: temperature profiles derived from lidar measurements (dots, red line), compared with temperatures measured by radiosonde (black line). Right: difference between radiosonde and lidar temperatures.

profile shown at the top was derived from RB line shapes sampled with 93 points separated by 125 MHz, leading to a frequency range of about 11.6 GHz and a measurement time of 28 min (12:20–12:48 UTC). The profile shown at the bottom was derived from RB line shapes sampled with 44 points separated by 250 MHz, reducing the measurement time to 14 min (13:17–13:31 UTC). A few RB spectra of the latter measurement are shown in Fig. 2. The range gate size was vertically adapted between 0.3 and 2.2 km to keep the number of received photons large enough to minimize the statistical error. Both temperature profiles are compared with radiosonde temperatures (Fig. 3, black line), launched at 12:00 from Oberschleißheim ($\approx$27 km distance from lidar).

The statistical error of the obtained temperature values (Fig. 3, error bars) is calculated by applying a maximum likelihood estimator (MLE) and considering solely Poisson noise on the measured data points. As discussed in [21], the width w_g ($w_g = \text{FWHM}/(8 \ln 2)^{1/2}$) of a Gaussian line shape, including Poisson noise, can be determined with a standard deviation $\sigma_{w_g} = w_g \cdot (2N)^{(-1/2)}$, where N is the number of detected photoelectrons. In this Letter, a similar approach was applied to derive the uncertainty of the width determined from the measured line shape [MLE for Eq. (1) but approximating $\mathcal{S}$ with a Gaussian line shape], which was additionally converted to the uncertainty of the determined temperature. In doing so, the statistical uncertainty σ_T (in Kelvin) of the derived temperature T (in Kelvin) is described by

$$\sigma_T = (189.43 \text{ K} + 1.21 \cdot T) \cdot N^{(-1/2)}. \qquad (4)$$

From the above equation, it can be seen that about 3×10^5 photoelectrons have to be detected to reach a statistical uncertainty of $\sigma_T = 1$ K.

The temperature profile shown in Fig. 3 (top) was obtained during noon and shows a good agreement to radiosonde temperatures. The profiles range from 2 to 15.3 km with a vertical resolution between 0.3 and 2.2 km. The temperature difference reaches up to 5 K within the boundary layer and is smaller than 2.5 K above. The inversion layer at 3 km, as well as the transition to the tropopause, is obvious. The statistical error (Eq. 4) varies from 0.15 K (at 2 km) to 1.5 K (at 15 km). The profile shown in Fig. 3 (bottom), however, shows larger systematic errors in regions of strong particle scattering. This can be seen from discrepancies in the boundary layer ($\approx$0–4 km), and even stronger at a cirrus cloud at 11 km, where the deviation to radiosonde temperature is almost 25 K. Although the influence of particle scattering was considered within the temperature retrieval (Eq. 3), uncertainties are caused by temporal variations in the aerosol load during line shape sampling. Simulations confirm that discrepancies of larger than 20 K can occur if the particle scattering is not constant within the sampling process. In addition, it has to be pointed out that an FPI resolution of 1.7 GHz (FWHM) is not well-suited to resolving the influence of particle scattering on the RB spectrum. Furthermore, discrepancies in the boundary layer might be caused by an incomplete overlap between the laser and the telescope FOV within this region. Thus, it can be concluded that, although very promising for clear air conditions, the suggested approach still suffers from the influence of particle scattering.

To improve this situation, an instrument that is able to sample the entire RB line shape simultaneously without any scanning procedures is proposed. This can be realized by imaging techniques such as, for instance, resolving the RB spectrum with a Fizeau interferometer and imaging the throughput on a multichannel PMT array. By using such a detector, even a varying aerosol load would not negatively influence the temperature retrieval. Furthermore, by designing the Fizeau interferometer with higher resolution, the aerosol peak can be better distinguished from the RB spectrum, which will additionally improve the temperature retrieval in regions of larger particle scattering. In addition to that, it is thinkable to design a hybrid system to measure temperature profiles that uses both Raman scattering in cloudy conditions and RB scattering during daytime and cloudless conditions.

Currently, both theoretical and practical work concerning these issues is in progress.

References

1. M. Alpers, R. Eixmann, C. Fricke-Begemann, M. Greding, and J. Höffner, Atmos. Chem. Phys. **4**, 793 (2004).
2. A. Behrendt, T. Nakamura, and T. Tsuda, Appl. Opt. **43**, 2930 (2004).
3. M. Radlach, A. Behrendt, and V. Wulfmeyer, Atmos. Chem. Phys. **8**, 159 (2008).
4. A. Behrendt and J. Reichardt, Appl. Opt. **39**, 1372 (2000).
5. M. Fraczek, A. Behrendt, and N. Schmitt, Appl. Opt. **51**, 148 (2012).
6. P. Di Girolamo, A. Behrendt, and V. Wulfmeyer, Appl. Opt. **45**, 2474 (2006).
7. B. Witschas, in *Atmospheric Physics: Background—Methods—Trends*, U. Schumann, ed. (Springer, 2012), pp. 69–83.
8. R. L. Schwiesow and L. Lading, Appl. Opt. **20**, 1972 (1981).
9. C. Y. She, R. J. Alvarez II, L. M. Caldwell, and D. A. Krueger, Opt. Lett. **17**, 541 (1992).
10. R. Alvarez, L. Caldwell, P. Wolyn, D. Krueger, T. McKee, and C. She, J. Atmos. Ocean. Technol. **10**, 546 (1993).
11. G. Tenti, C. Boley, and R. Desai, Can. J. Phys. **52**, 285 (1974).
12. J. Hair, L. Caldwell, D. Krueger, and C. She, Appl. Opt. **40**, 5280 (2001).
13. D. Hua, M. Uchida, and T. Kobayashi, Appl. Opt. **44**, 1315 (2005).
14. B. Witschas, Appl. Opt. **50**, 267 (2011).
15. B. Witschas, Appl. Opt. **50**, 5758 (2011).
16. European Space Agency, ESA SP-1311 (European Space Research and Technology Centre, 2008).
17. O. Reitebuch, C. Lemmerz, E. Nagel, and U. Paffrath, J. Atmos. Ocean. Technol. **26**, 2501 (2009).
18. B. Witschas, C. Lemmerz, and O. Reitebuch, Appl. Opt. **51**, 6207 (2012).
19. B. Witschas, M. O. Vieitez, E.-J. van Duijn, O. Reitebuch, W. van de Water, and W. Ubachs, Appl. Opt. **49**, 4217 (2010).
20. M. Vieitez, E.-J. van Duijn, W. Ubachs, B. Witschas, A. Meijer, A. de Wijn, N. Dam, and W. van de Water, Phys. Rev. A **82**, 1094 (2010).
21. N. Hagen, M. Kupinski, and E. L. Dereniak, Appl. Opt. **46**, 5374 (2007).